

Document Version

Final published version

Licence

CC BY

Citation (APA)

Mishra, V., & Wu, J. (2026). Differentiable modelling and optimization of multi-planar slicing for multi-axis additive manufacturing. *Structural and Multidisciplinary Optimization*, 69(2), Article 31. <https://doi.org/10.1007/s00158-025-04240-3>

Important note

To cite this publication, please use the final published version (if applicable).
Please check the document version above.

Copyright

In case the licence states “Dutch Copyright Act (Article 25fa)”, this publication was made available Green Open Access via the TU Delft Institutional Repository pursuant to Dutch Copyright Act (Article 25fa, the Taverne amendment). This provision does not affect copyright ownership.
Unless copyright is transferred by contract or statute, it remains with the copyright holder.

Sharing and reuse

Other than for strictly personal use, it is not permitted to download, forward or distribute the text or part of it, without the consent of the author(s) and/or copyright holder(s), unless the work is under an open content license such as Creative Commons.

Takedown policy

Please contact us and provide details if you believe this document breaches copyrights.
We will remove access to the work immediately and investigate your claim.



Differentiable modelling and optimization of multi-planar slicing for multi-axis additive manufacturing

Vibhas Mishra¹ · Jun Wu¹

Received: 8 May 2025 / Revised: 8 October 2025 / Accepted: 17 December 2025 / Published online: 20 January 2026
© The Author(s) 2026

Abstract

Multi-planar deposition, enabled by multi-axis additive manufacturing, provides an opportunity to address challenging issues in wire arc additive manufacturing, such as residual stresses and distortions. This strategy involves sequentially building sub-parts, by depositing material in each sub-part with a distinct printing direction. In this paper, we present a novel continuous and differentiable formulation to model the multi-planar slicing strategy. The strategy is parameterized using a pseudo-time field, which allows the part to be segmented into sub-parts. An orientation field is used to define the distinct printing direction for each sub-part. This differentiable formulation enables gradient-based optimization of the multi-planar slicing. We apply the method to reduce distortion in wire arc additive manufacturing. The method is tested on several numerical examples with complex geometries, including holes, overhangs, and underhangs. Numerical results show that the multi-planar deposition approach reduces distortion by an order of magnitude compared with the conventional planar strategy.

Keywords Multi-axis additive manufacturing · Multi-planar slicing · Fabrication sequence optimization · Wire arc additive manufacturing · Thermally induced distortion

1 Introduction

Additive manufacturing (AM), commonly known as 3D printing, has seen rapid advancements over the past two decades. Traditionally, AM systems typically involve three translational degrees of freedom to construct 3D parts. A notable recent innovation is the integration of rotational degrees of freedom, using robotic arms or turn-tilt tables (Lettori et al. 2022). These systems, often referred to as multi-axis AM systems, offer exciting new opportunities to address challenges associated with conventional 3D printing. Central to unlocking the potential of multi-axis AM is slicing, a crucial step in transforming 3D digital models into physical parts. Slicing involves decomposing a 3D digital model into a series of layers (Livesu et al. 2017). In conventional 3D printing, the layers are planar with a fixed orientation. In con-

trast, multi-axis AM systems enable orientation adjustments during fabrication by rotating the build plate, the nozzle, or both.

Figure 1 illustrates three slicing strategies. On the left (Fig. 1a), the layers are planar and maintain a fixed orientation. On the right (Fig. 1c), the layers are curved, and this requires continuous rotation of the build plate and/or nozzle (Dai et al. 2018; Zhang et al. 2022). This curved fabrication fully leverages the motion flexibility of multi-axis AM systems, but it introduces significant complexities in slicing and robot motion planning, such as avoiding collisions. Additionally, varying orientation and thickness along a curved layer demands continuous adjustment of process parameters (e.g., travel speed, feed rate), which presents challenges for ensuring consistent fabrication quality. In Fig. 1b, the 3D part is divided into two sub-parts, each consisting of a set of planar layers with a distinct orientation. This multi-planar slicing strategy (also referred to as multi-direction slicing) strikes a practical balance, offering enhanced flexibility over planar printing with minimal increase in complexity, and reducing the challenges associated with non-planar deposition, which may demand constant adaptation of process parameters.

In this paper, we focus on multi-planar slicing and explore its potential to address pressing challenges in robotic 3D

Communicated by Kai James.

✉ Jun Wu
j.wu-1@tudelft.nl

¹ Sustainable Design Engineering, Faculty of Industrial Design Engineering, Delft University of Technology, Landbergstraat 15, 2628CE Delft, Zuid-Holland, The Netherlands

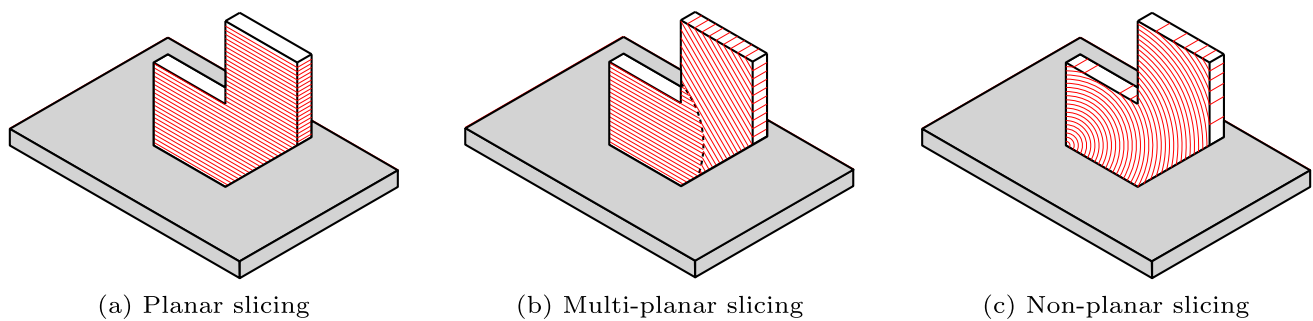


Fig. 1 Schematic of **a** planar, **b** multi-planar, and **c** non-planar slicing for additive manufacturing

metal printing, such as Wire-Arc Additive Manufacturing (WAAM). WAAM combines traditional welding methods with additive manufacturing principles. It is a promising technique for producing large, customized metal parts with complex geometries. However, its widespread adoption in critical industries is often hindered by residual stresses and distortions that arise during the directed energy deposition process. Previous efforts to mitigate these undesirable effects include optimizing process parameters to control thermal gradients (Rodrigues et al. 2019; Jafari et al. 2021) and post-processing, such as heat treatment to reduce residual stresses (Shen et al. 2022; Elmer et al. 2022). Despite these efforts, challenges persist in achieving a consistent quality of parts, particularly for complex geometries. In this paper, we propose addressing these challenges through a multi-planar material deposition strategy. This strategy complements the previous focus on optimizing process parameters and post-processing techniques, offering a new direction to improve the quality and precision of WAAM-produced parts.

Our objective is to provide a computational framework to optimize multi-planar slicing in order to minimize distortion caused by the fabrication process. Multi-planar slicing involves determining how a part is decomposed into sub-parts and selecting the printing direction for each sub-part. Part decomposition is a classic problem in design for additive manufacturing (Singh and Dutta 2001), and has been discussed in a few review articles (Jafari et al. 2021; Lettori et al. 2022; Oh et al. 2018). Decomposition is particularly necessary for large parts that exceed the working volume of the 3D printer (Luo et al. 2012; Yao et al. 2015; Jiang et al. 2017), as these parts must be produced in smaller segments and subsequently assembled. When combined with multi-axis printing, decomposition can reduce or even eliminate the need for support structures (Wu et al. 2017; Xu et al. 2018; Wu et al. 2019; Gao et al. 2019; Xiao and Joshi 2020). To address the relatively weaker interfaces between sub-parts, structural analysis has been used to guide the decomposition process, avoiding regions of high stress (Yao et al. 2015; Bi et al. 2023). Additionally, decomposition must consider the accessibility of the nozzle to ensure that each sub-part can be

manufactured with a collision-free robotic motion (Murtezaoglu et al. 2018; Guo et al. 2025).

Our work differentiates itself from prior research on part decomposition and multi-planar slicing in two significant ways. First, we shift the focus from manufacturability to the quality of manufacturing, and specifically aim at minimizing thermally induced distortion. Achieving this objective requires simulating the fabrication process and predicting the distortion at each iteration of the optimization process. Consequently, computational efficiency becomes critical for distortion prediction. Towards this end, we employ a simplified process model based on the inherent strain method. Originally developed for welding simulations (Ueda et al. 1975), this method substitutes computationally intensive transient thermomechanical analyses with an efficient quasi-static mechanical analysis to estimate deformation. Due to its computational efficiency, the inherent strain method has been adopted for modeling AM processes (Ma et al. 2016; Munro et al. 2019; Liang et al. 2019; Chen et al. 2019; Prabhune and Suresh 2020). It has also been successfully integrated into structural topology optimization to minimize distortion (Allaire and Jakabčín 2018; Pellens et al. 2020; Misiun et al. 2021; Miki and Yamada 2021). Unlike its typical use in structural optimization, in this work, we employ the inherent strain method to optimize the fabrication sequence.

Second, unlike prior approaches that explicitly represent segmentation boundaries and optimize them using recursive subdivision schemes (e.g., Wu et al. 2019), our method represents multi-planar slicing and the corresponding fabrication process using continuous and differentiable functions. This enables efficient gradient computation, facilitating gradient-based numerical optimization. Our framework builds on the recently developed space-time topology optimization approach and its extensions (Wang et al. 2020, 2023, 2024; Wu et al. 2024, 2025), which represents the fabrication sequence using a continuous pseudo-time field. While initially designed for curved fabrication, where segments correspond to curved layers, we adapt and extend it to multi-planar slicing. Here, each segment represents a sub-part that consists of many planar layers. Additionally, we introduce an

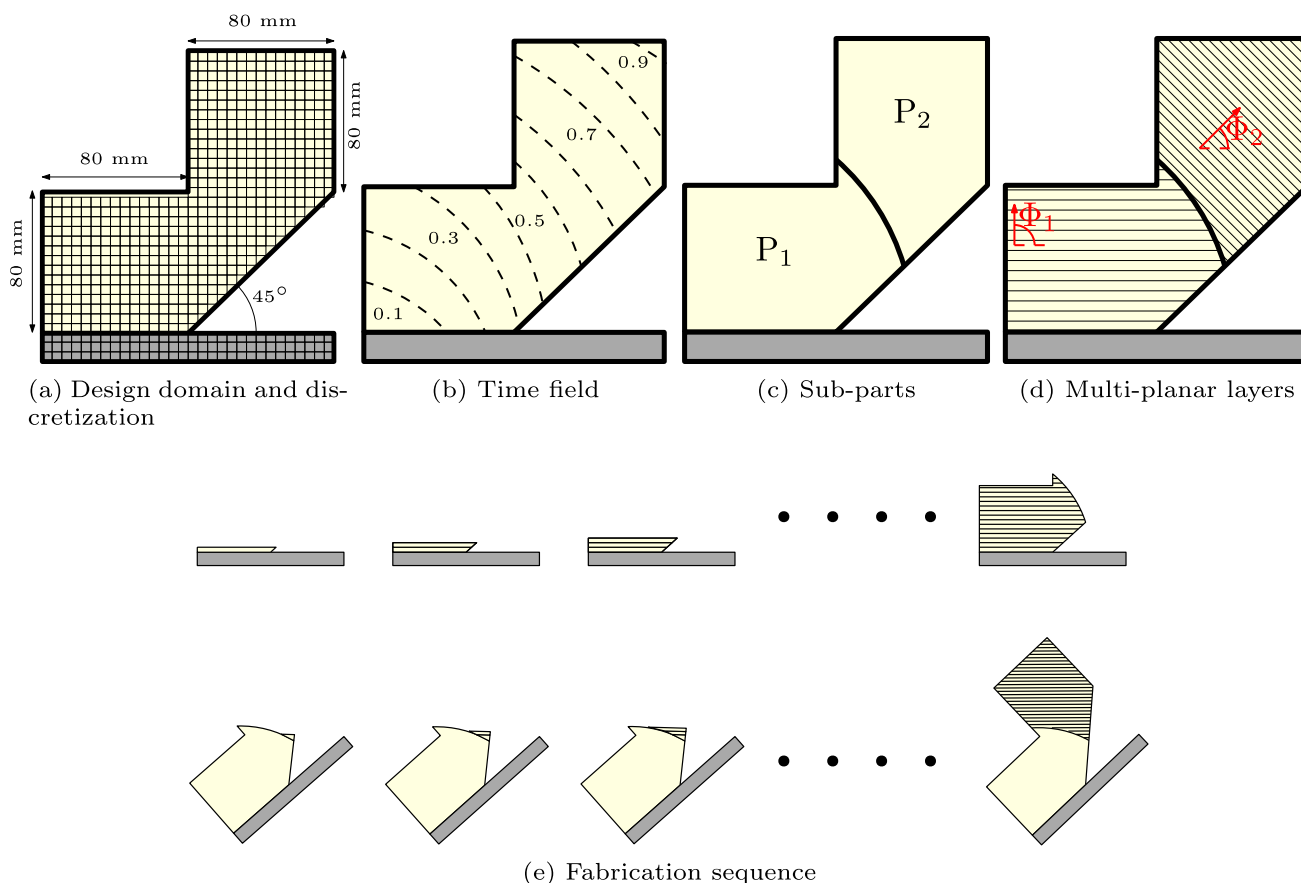


Fig. 2 Schematic of multi-planar slicing for robotic-assisted additive manufacturing. **a** Thin-walled structure and substrate represented by finite elements. **b** Pseudo-time field indicating the fabrication sequence. **c** Sub-parts obtained by segmenting the pseudo-time field. **d** Planar layer fabrication of each sub-part with a distinct print direction. **e** Fabrication

sequence of sub-parts and their respective layers. The top and bottom rows represent the fabrication of the first and second sub-parts, respectively. Note that after the completion of the first sub-part, the substrate is rotated such that the layers of the second sub-part are horizontal

orientation variable to encode the printing direction of each sub-part. This enriched formulation provides an optimization framework for determining the part decomposition and orientation of sub-parts. We further demonstrate the method’s extensibility by incorporating manufacturability considerations related to the shape and orientation of segmentation boundaries.

The remainder of this paper is structured as follows. Section 2 provides a detailed description of the differentiable modeling approach for multi-planar slicing. Section 3 discusses the distortion calculation and the formulation of the optimization problem. Sect. 4 compares different optimization setups and demonstrates the effectiveness of multi-planar slicing through multiple numerical examples, including consideration of manufacturability. Finally, Sect. 5 summarizes the key findings of this study.

2 Multi-planar slicing

Given the design of a part, our method aims to find a decomposition of the part and the distinct print direction per sub-part. To achieve this, we introduce two sets of variables: a pseudo-time field (τ), and a set of orientation angles, $[\Phi_1, \Phi_2, \dots, \Phi_{N_p}]$, where Φ_i represents the print direction of the i -th sub-part, and N_p is the number of sub-parts, which the user specifies.

The pseudo-time field is defined on a finite element discretization of the part (Ω), as schematically shown in Fig. 2a and b. Each element takes a time value between 0.0 and 1.0, where a larger value indicates the element materializes later in the fabrication process. The purpose of the pseudo-time field is to decompose the part into sub-parts. For instance, as illustrated in Fig. 2c, the threshold of 0.5 segments the part into two separate sub-parts. The elements where the associated time values are smaller than or equal to 0.5 belong to the

first sub-part (P_1), and the elements with values larger than 0.5 are in the second sub-part (P_2).

For each sub-part, the print direction uniquely defines a set of planar layers. We consider a virtual slicing plane orthogonal to the print direction. The slicing plane starts from a reference point (e.g., the bottom left of the part) and propagates along the print direction at a constant step size, generating a series of planar layers. Figure 2d illustrates the planar layers in sub-parts. The step size represents the thickness of the layer in the AM process. Figure 2e illustrates the fabrication sequence, where the top and bottom rows show the layer-by-layer deposition of the first and second sub-parts, respectively. We note that for each sub-part, the substrate can be rotated to ensure the layers remain horizontal, typically achieved using a turn-tilt table.

2.1 Pseudo-time field

We utilize a pseudo-time field to encode the fabrication sequence. To mimic the additive process, this field must be continuous and monotonically increasing from the designated starting point (e.g., the build plate). To enforce these properties, we adopt the PDE-based regularization approach proposed by Wang et al. (2024). Instead of optimizing the pseudo-time field directly, we introduce an auxiliary field as optimization variables, from which the pseudo-time field is derived by solving a partial differential equation (PDE). Specifically, the PDE represents a fictitious thermal diffusion process: a heat source is applied to the build plate, and the temperature decreases smoothly throughout the domain. By optimizing element-wise thermal conductivities, we obtain a smooth temperature distribution, which is then interpreted as the pseudo-time field.

The PDE-based regularization works as follows. We discretize the design domain by a structured finite element mesh, and assign each element a design variable, ξ_e , representing the thermal conductivity of that element (e). The element-level thermal conductivity matrix is obtained by an interpretation function, similar to the modified SIMP commonly used in density-based topology optimization (Bendsøe and Sigmund 2004),

$$\{\mathbf{k}_T\}_e = (\kappa_{\min} + \xi_e(\kappa_0 - \kappa_{\min}))\{\mathbf{k}_T\}. \quad (1)$$

Here κ_0 and κ_{\min} are the maximum and minimum values of the thermal conductivity, respectively. We choose $\kappa_0 = 1$ and $\kappa_{\min} = 1 \times 10^{-9}$. $\{\mathbf{k}_T\}$ is the element conductivity matrix for an element with unit conductivity. The subscript e represents the element level matrix of element e with the design variable ξ_e .

The heat equation describes steady-state thermal conduction in a heterogeneous medium, characterized by spatially varying thermal diffusivity and the presence of a drain term.

Detailed formulations can be found in Wang et al. (2024). In its discretized form, the equation is expressed as

$$\mathbf{K}_T \mathbf{T} = \mathbf{b}, \quad (2)$$

where the global system matrix \mathbf{K}_T is constructed from contributions of the thermal conductivity matrix and the drain term. \mathbf{T} is the global nodal temperature vector, and \mathbf{b} is the global heat load vector. We impose Dirichlet boundary conditions on the nodes that represent the substrate domain. The temperature on these nodes is constant and takes a value of 1. The initial temperature values at other nodes are equal to 0. This results in a temperature distribution with values between 0 and 1. After solving the heat equation, we transform the temperature from nodes (\mathbf{T}) to elements (\mathbb{T}) by bilinear interpolation,

$$\mathbb{T} = \mathbf{A} \mathbf{T}, \quad (3)$$

where \mathbf{A} is the transformation matrix. Effectively, the elemental temperature is the mean of the temperature values of its corresponding nodes.

The temperature decreases from the substrate within the domain. We reverse the order of the scalar field by defining the pseudo-time field as

$$\tau = \mathbf{1} - \mathbb{T}. \quad (4)$$

In this way, the pseudo-time near the substrate is close to zero, representing the early stage in the fabrication process.

To illustrate the workflow of the proposed process, we solve the heat equation on a numerical example. The nodal temperature, elemental temperature, and the pseudo-time fields, with isolines, are shown in Fig. 3. High temperature values are near the substrate and low temperatures are away from it. The pseudo-time field complements it, indicating early deposition near the substrate and later deposition away from it.

2.2 Part decomposition

From the pseudo-time field, the part is segmented into sub-parts by prescribed timestamps. Assuming a total of N_p sub-parts, we denote the corresponding timestamps by $\tau_0, \tau_1, \dots, \tau_{N_p}$. Each timestamp, τ_i , divides the part into two regions: one that has already been fabricated up to τ_i , and another that remains to be fabricated. For gradient-based numerical optimization, the division is realized via an inverted Heaviside function,

$$\mathbf{H}(\tau, \tau_i) = 1 - \frac{1}{1 + \exp(-k_1(\tau - \tau_i))}. \quad (5)$$

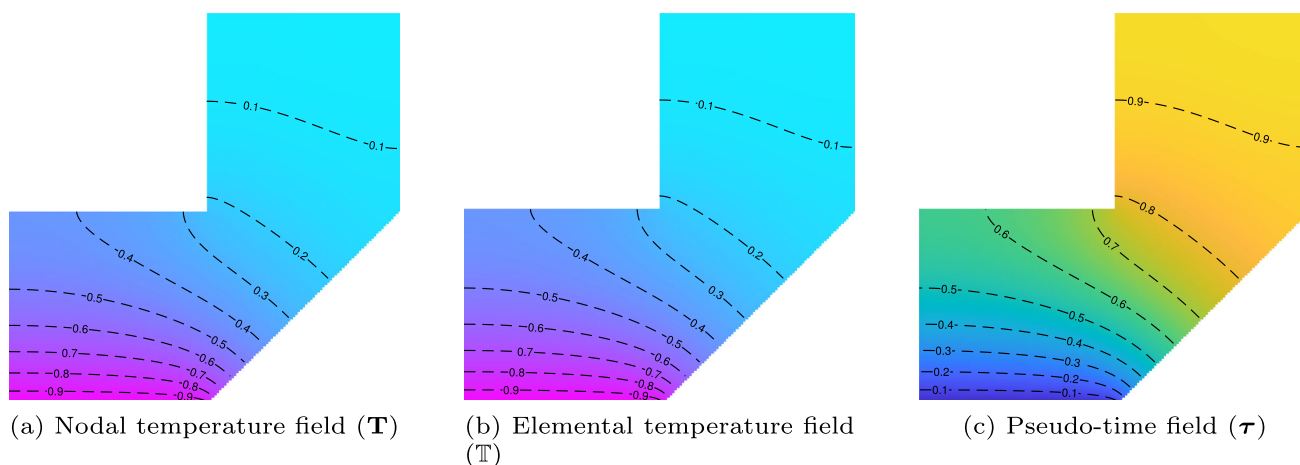


Fig. 3 Schematic of pseudo-time field generation. **a** Nodal temperature field \mathbf{T} , computed by solving the fictitious heat conduction problem. **b** Elemental temperature field \mathbb{T} , obtained via bilinear interpolation of \mathbf{T} . **c** Pseudo-time field τ , derived through complementation $\tau = 1 - \mathbb{T}$

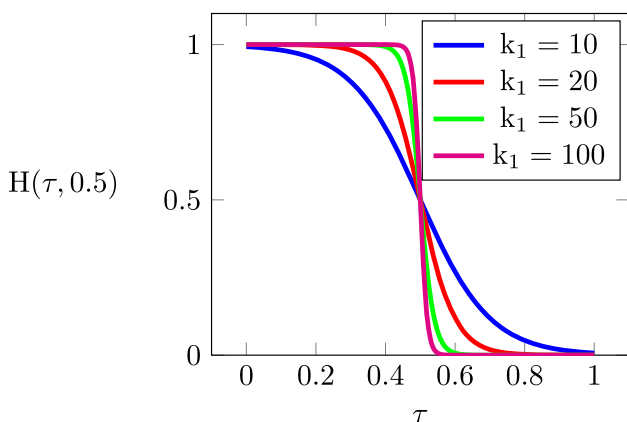


Fig. 4 The effect of parameter k_1 on the shape of the inverted Heaviside function

This function differentially transforms a time field into a quasi-binary distribution. It maps time values smaller than the timestamp τ_i to values close to 1, and larger ones to values close to 0. Being continuous and differentiable, this function allows for smooth transitions, with the parameter k_1 controlling the sharpness of the Heaviside projection. Figure 4 illustrates the effect of this parameter on the function’s shape. In our study, the default value of k_1 is = 100.

The elements with pseudo-time values between two successive timestamps (τ_{i-1} and τ_i) constitute a sub-part, P_i . These elements are identified by the difference between the Heaviside function that takes τ_{i-1} and τ_i as input,

$$E_{P_i} = \mathbf{H}(\tau, \tau_i) - \mathbf{H}(\tau, \tau_{i-1}). \tag{6}$$

E_{P_i} is again a scalar field, with values close to 1 for elements belonging to sub-part P_i and 0 elsewhere.

For illustrative purposes, the previous part is divided into 3 sub-parts, by timestamps 0, 0.3, 0.7, and 1.0. In Fig. 5a, the

solid isolines correspond to the timestamp values. Figure 5b-d display the three sub-parts. A smooth but narrow transition at the interface between sub-parts can be observed. They result from the continuous nature of the smoothed Heaviside function.

2.3 Planar slicing of sub-parts

The next computational step is to slice each sub-part into planar layers along its designated print direction. This process involves two major steps. First, the domain of the entire part is sliced according to the print direction. Then, the planar layers for each sub-part are determined by restricting the slices to the sub-part’s domain.

As illustrated in Fig. 6, the planar layers are oriented orthogonally to the print direction, which is defined by the orientation variable Φ_i , representing the angle between the print direction and the x -axis. Given the print direction, we define the line that passes through the origin and is orthogonal to the print direction as a reference. This reference line then sweeps through the entire domain with a constant step size, determined by a user-specified layer thickness. Depending on the print direction, the sweeping may have to proceed both along the print direction and its negative direction to cover the domain of the entire part.

The elements located between two consecutive lines form a layer. To determine this, we first compute the distance from the centroid of each element to the reference line,

$$S_i = \mathbf{Y} \sin \Phi_i + \mathbf{X} \cos \Phi_i, \quad i = 1, \dots, N_P. \tag{7}$$

Here, \mathbf{X} and \mathbf{Y} are the arrays of x and y coordinates of all elements, respectively. S_i represents the distance from each element to the reference line corresponding to the orientation Φ_i . We note that the distance may have positive or negative

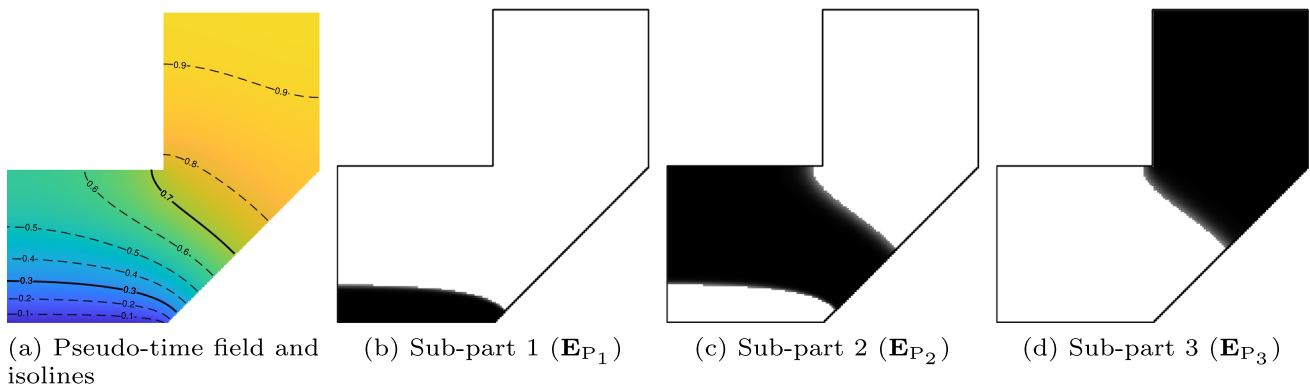


Fig. 5 The isolines corresponding to the prescribed timestamps, indicated by the solid lines, segment the pseudo-time field (a), and thus the entire part, into three sub-parts (b, c, d)

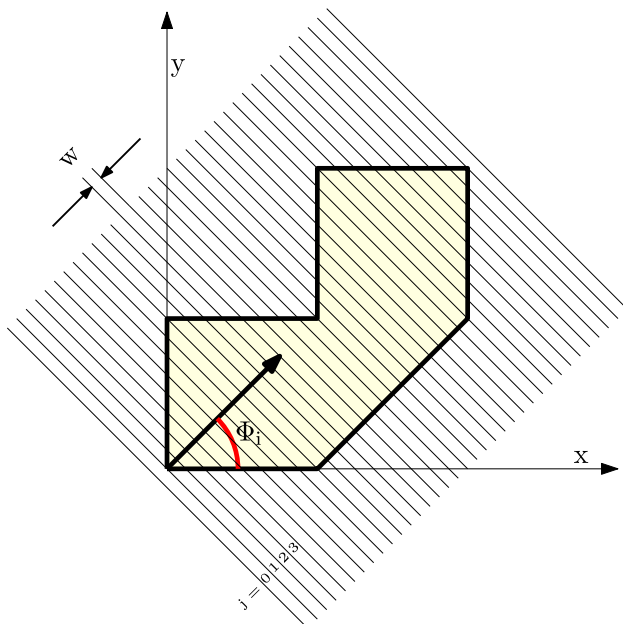


Fig. 6 Planar slicing over the domain of the entire part, according to the print direction Φ_i

values. A negative value means that the element is below the reference line, i.e., opposite to the print direction.

From its distance to the reference line and the layer thickness, we determine in which layer an element is located. Denoting the layer index by j , elements with a distance value between $(j - 1) \times w$ and $j \times w$ fall within the j -th layer. Here, w is the layer thickness. This is achieved through a differentiable projection function,

$$E_{L_{ij}} = 1 - \frac{1}{1 + \exp\left(k_2 \left(1 - \frac{4}{w^2} (S_i - 0.5w - w)(j - 1)\right)^2\right)} \tag{8}$$

This function projects the distance S_i to 1 for values between $(j - 1) \times w$ and $j \times w$, and to 0 otherwise. Like the previously introduced Heaviside function, it involves a parameter k_2 , which controls the sharpness of the projection. This parameter takes a default value of $k_2 = 100$. Figure 7 illustrates the layer of $j = 1$ for two different thicknesses, $w = 1$ on the left, and $w = 2$ on the right.

We note that the layer index j is an integer between $j_{\min} = \lfloor \min(S_i)/w \rfloor$ and $j_{\max} = \lceil \max(S_i)/w \rceil$. As the distance S_i may take negative values, so can the layer index j . The distance values and thus the layer index differ for each orientation variable Φ_i . When the shape and size of the domain and the layer thickness are prescribed, the number of layers is then determined by the orientation variable. We denote the maximum number of layers by N_L .

After slicing the domain of the entire part, we restrict the slicing to the domain of the i -th sub-part. This is achieved by entry-wise multiplication of two fields,

$$E_{L_{ij}}^{P_i} = E_{P_i} \circ E_{L_{ij}} \tag{9}$$

Recall that E_{P_i} represents the i -th sub-part. $E_{L_{ij}}^{P_i}$ is a scalar field with values equal to 1 for elements in layer L_{ij} within sub-part P_i , and 0 otherwise. $E_{L_{ij}}^{P_i}$ with $i \in [1, N_p]$ and $j \in [j_{\min}, j_{\max}]$ encodes the multi-planar slicing, i.e., both the sub-parts and successive layers in each sub-part. Figure 8 visualizes $E_{L_{ij}}$ and $E_{L_{ij}}^{P_i}$ for three layers, each in a distinct sub-part. Here, the sub-parts correspond to the decomposition in Fig. 5. The three orientation variables are $\Phi_1 = \pi/2$, $\Phi_2 = \pi/4$, $\Phi_3 = \pi/2$, and the layer thickness is set to $w = 3$ mm.

Fig. 7 Projection function for the j -th layer ($j = 1$ in this illustration) with a layer thickness $w = 1$ on the left and $w = 2$ on the right

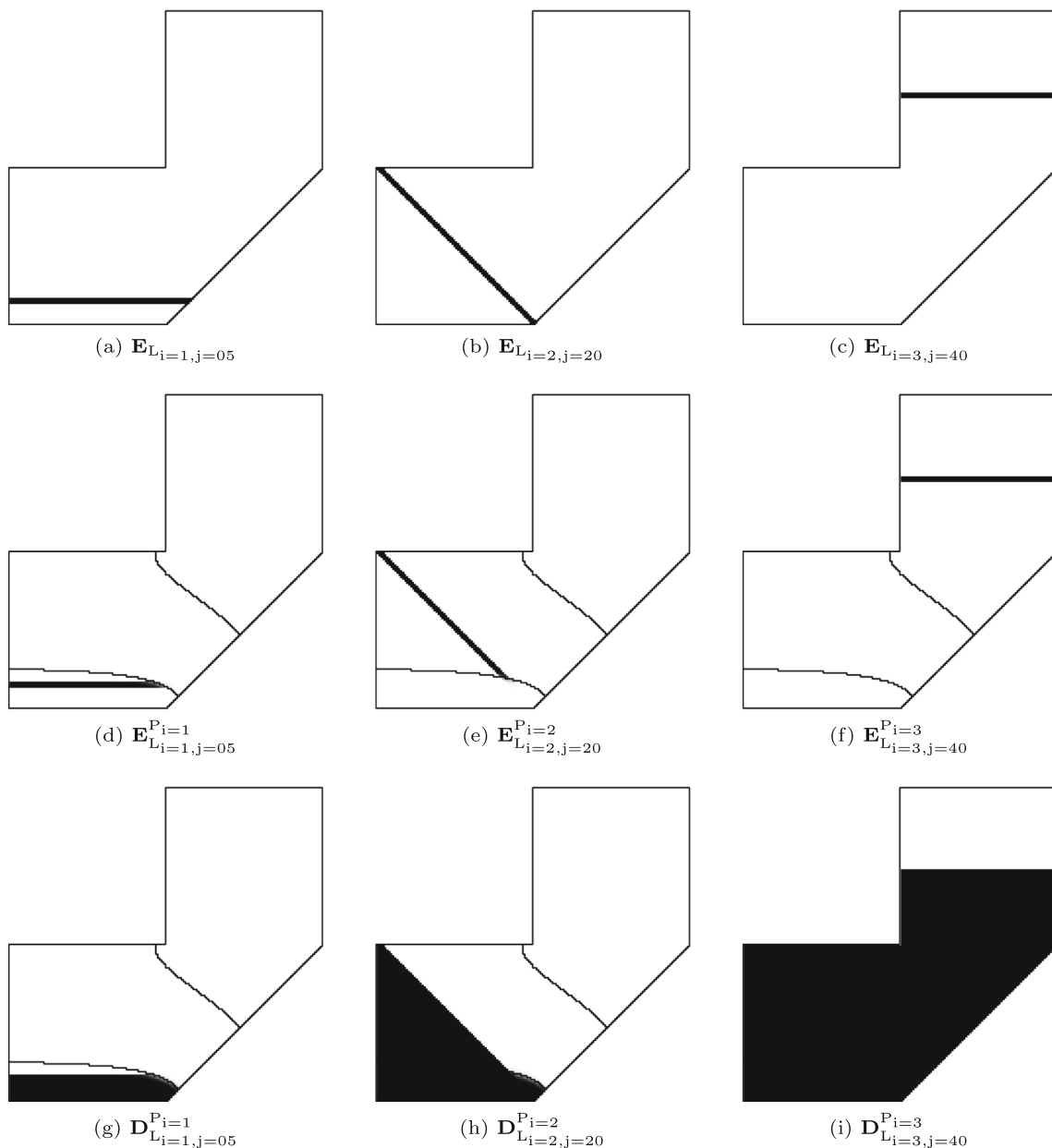
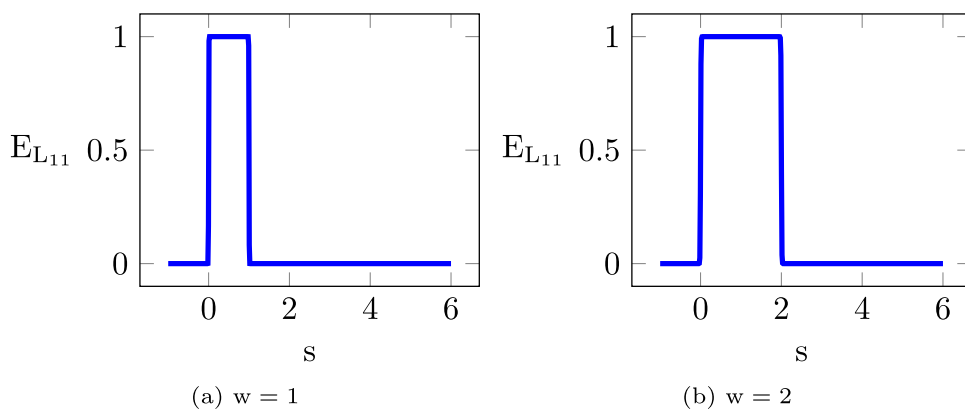


Fig. 8 Top row: Three planar layers, each orthogonal to a distinct print direction defined over the entire domain. Middle row: The layers considering the shape and size of the sub-part. Bottom row: The intermediate structure that has been deposited up to and including the current layer

3 Distortion calculation and optimization problem

We employ the multi-planar slicing strategy to minimize thermally induced distortion in wire arc additive manufacturing. This section first describes the computation of the distortion, followed by the formulation of the corresponding optimization problem.

3.1 Distortion calculation

In this work, we use the inherent strain method to simulate the thermally-induced mechanical load in the additive manufacturing process. This method assumes static mechanical loads and neglects transient thermomechanical effects due to temperature-dependent material properties. When a new layer is deposited, the inherent strain of elements belonging to this layer is activated, resulting in the deformation of previous sub-parts and layers.

The magnitude of the inherent strain is related to the thermal expansion coefficient of the material (α_{mat}), and the change in temperature,

$$\epsilon_{ihs} = \alpha_{mat}(T_m - T_0). \tag{10}$$

T_m and T_0 are the melting and inter-layer temperatures, respectively. Applying the inherent strain to a finite element, in Voigt notation, the strain is represented by

$$\epsilon_{ihs} = [-\epsilon_{ihs} \quad -\epsilon_{ihs} \quad 0]^T. \tag{11}$$

The corresponding mechanical load is calculated as

$$\mathbf{f}_{ihs} = \mathbf{B}^T \mathbf{D}_0 \epsilon_{ihs}. \tag{12}$$

\mathbf{f}_{ihs} is the element-level load vector due to the inherent strain. \mathbf{B} and \mathbf{D}_0 are the strain–displacement relationship and constitutive matrix of the material, respectively. To simulate the additive manufacturing process, we repeatedly apply the inherent strain, each time to elements associated with a new layer. Identifying the new layer by $\mathbf{E}_{L_{ij}}^{P_i}$ (i.e., layer L_{ij} within the sub-part P_i), the corresponding load vector is

$$\mathbf{f}_{L_{ij}}^{P_i} = \left(\mathbf{E}_{L_{ij}}^{P_i} \right)^q \mathbf{f}_{ihs}. \tag{13}$$

Here, q is a penalization coefficient. It penalizes elements with low values of $\mathbf{E}_{L_{ij}}^{P_i}$. The assembly of element-level load vectors generates a global load vector, $\mathbf{F}_{L_{ij}}^{P_i}$.

The load vector acts on the current intermediate structure that has been deposited up to and including this new layer (cf. Fig. 8 bottom row). This intermediate structure consists

of previous sub-parts and previous layers within the current sub-part. Mathematically, it is identified by

$$\mathbf{D}_{L_{ij}}^{P_i} = \mathbf{H}(\tau, \tau_{i-1}) + \sum_{k=j_{min}}^j \mathbf{E}_{L_{ik}}^{P_i}. \tag{14}$$

On the right-hand side of the equation, the first term corresponds to the previous sub-parts, and the second term to the previous layers in the current sub-part.

The stiffness matrix of the intermediate structure is calculated according to the Solid Isotropic Material with Interpolation (SIMP) model, which is commonly used in density-based topology optimization. Specifically, the element stiffness matrix is

$$\mathbf{k}_{L_{ij}}^{P_i} = \left(E_{min} + \left(D_{L_{ij}}^{P_i} \right)^p (E_0 - E_{min}) \right) \mathbf{k}_0. \tag{15}$$

E_{min} and E_0 are Young’s modulus values of the void and material, respectively. p is a penalization coefficient on the stiffness matrix. \mathbf{k}_0 is the stiffness matrix of the material. Assembling the element-level matrices generates the corresponding global stiffness matrix, denoted as $\mathbf{K}_{L_{ij}}^{P_i}$.

The (incremental) distortion of the intermediate structure, due to the mechanical load of the new layer, is obtained by solving the following state equation,

$$\mathbf{K}_{L_{ij}}^{P_i} \Delta \mathbf{u}_{L_{ij}}^{P_i} = \mathbf{F}_{L_{ij}}^{P_i}. \tag{16}$$

$\Delta \mathbf{u}_{L_{ij}}^{P_i}$ represents the incremental distortion due to the deposition of the layer L_{ij} within sub-part P_i . The total distortion is given as

$$\Delta \mathbf{u} = \sum_{i=1 \dots N_p} \sum_{j=j_{min} \dots j_{max}} \Delta \mathbf{u}_{L_{ij}}^{P_i}. \tag{17}$$

$\Delta \mathbf{u}$ is the accumulation of the distortion by all layers.

Figure 9 illustrates the multi-planar deposition strategy and the resulting accumulated distortion from the previous numerical example. As depicted in Fig. 9a, the complete part is constructed sequentially by depositing blue-, orange-, and yellow-coloured sub-parts. Figure 9b presents the distortion according to the multi-planar sequence, where the orange and blue regions represent the distorted and reference shapes, respectively.

3.2 Optimization problem

The proposed formulation models the multi-planar slicing and its resulting thermally-induced distortion. We introduce a gradient-based approach to optimize the multi-planar slicing in order to minimize the distortion for a given design. This strategy is parameterized by two independent sets of design

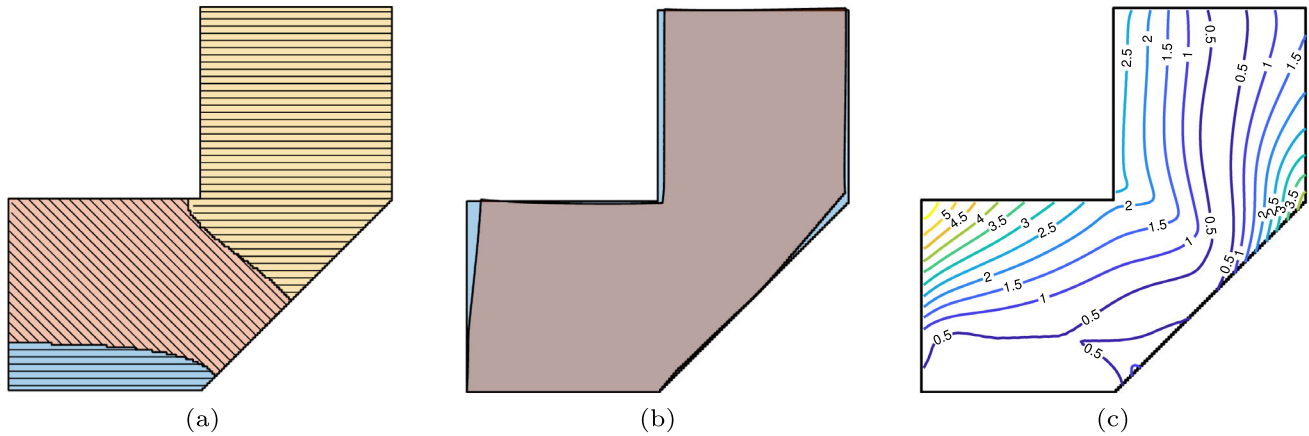


Fig. 9 **a** The modeled multi-planar strategy using the presented differentiable mathematical formulation. **b** Predicted distorted shape (orange) superimposed on the reference shape (blue). **c** The corresponding contour plot of the magnitude of the accumulated distortion

variables: local conductivities (ξ) and orientation (Φ). The optimization problem is formulated as follows.

$$\min_{\xi, \Phi} O = \sum_{i=1}^{N_p} \sum_{j=j_{\min}}^{j_{\max}} \left[\Delta \mathbf{u}_{L_{ij}}^{P_i} \right]^T \left[\Delta \mathbf{u}_{L_{ij}}^{P_i} \right]. \tag{18}$$

$$\text{s.t. } \mathbf{K}_{L_{ij}}^{P_i} \Delta \mathbf{u}_{L_{ij}}^{P_i} = \mathbf{F}_{L_{ij}}^{P_i}, \quad \forall i = 1 \dots N_p, \quad \forall j = 1 \dots N_L. \tag{19}$$

$$g_i = \frac{V_{P_i}}{V_0} - 1 \leq 0, \quad \forall i = 1 \dots N_p. \tag{20}$$

$$0 \leq \xi_e \leq 1, \quad \forall e = 1 \dots N_E. \tag{21}$$

$$\Phi_{\min} \leq \Phi_i \leq \Phi_{\max}, \quad \forall i = 1 \dots N_p. \tag{22}$$

Here, the objective function (O) is the aggregation of the distortion caused by every deposited layer. Equation (19) represents the state equation to determine the incremental distortion corresponding to the deposition of each new layer. Equation (20) represents the volume constraint imposed on each process interval. V_{P_i} is the volume of the i -th process interval, corresponding to the field of E_{P_i} . We assume in each process interval the same amount of material is processed, i.e., $V_0 = \frac{1}{N_p} V_D$, where V_D is the volume of the given shape. Equation (21) and Eq. (22) represent the bounds on the design variables.

To solve the optimization problem, the sensitivities of the objective function and the constraint function with respect to the design variables are required. The adjoint sensitivity analysis of the objective function is given in Appendix A.

4 Results

We have implemented the proposed method in MATLAB and tested it on multiple numerical examples. This section presents the results, analyzing optimization options (Sect. 4.1), incorporating manufacturability considerations (Sect. 4.2), and demonstrating multiple examples of varying geometric complexity (Sect. 4.3). In all numerical examples, the parameters are kept consistent, taking default values listed in Table 1, unless stated otherwise.

4.1 Optimization options

The first investigation is on the effect of orientation variables when the segmentation of the parts into sub-parts remains fixed during optimization. The solution to the optimization problem yields an optimized layer orientation for each sub-part that minimizes global distortion. Figure 10 shows a prescribed segmentation of the part into two sub-parts. The sequential deposition of the blue and orange-colored sub-parts realizes the whole part. Figure 10a and b illustrate two reference orientations, while Fig. 10c depicts the optimized orientations. In the middle row, Fig. 10d–f visualize the corresponding predicted distortion. The values in parentheses indicate the normalized value of the objective function, with Fig. 10a as the reference. Compared to the horizontal layers shown on the left, the optimized layer orientation reduces distortion by 87.8%. The distortion from the 45° layers is smaller than the horizontal layers but still 5.3 times larger than the optimized orientation. This comparison confirms that the orientation of the layers significantly influences the distortion objective. The bottom row, Fig. 10g–i, provides the contour plots of the accumulated distortion. Different printing strategies lead to varying patterns in the accumu-

Table 1 Default parameters used for the finite element modelling and optimization

Modelling and material properties		Optimization parameters	
Element size	1 mm × 1 mm	p	3
Element Type	Plane stress Q4	q	3
E_0	210 GPa	V_0	$(1/N_P)V_D$
E_{\min}	$10^{-9}E_0$	Φ_{\min}	0
Poisson's ratio (ν)	0.3	Φ_{\max}	$\pi/2$
Domain thickness	1 mm	w	3 mm
Thermal properties for inherent Strain calculation			
α_{mat}	$9 \times 10^{-6} / ^\circ\text{C}$	T_0	20 °C
T_m	1500 °C		

lated distortion, with the optimized strategy yielding a more intricate one.

The next investigation is the effect of part segmentation on the distortion objective. To this end, we fix the orientation variables while allowing the local conductivities to be optimized. The fixed orientation variables are the same as those shown in Fig. 10. Figure 11 shows the optimized part segmentation and the corresponding predicted distortions. Comparing these optimized results with those in Fig. 10, we observe that optimizing the segmentation reduces the distortion by 77.3%, 64.4%, and 40.9%, for the three prescribed orientations, respectively. This comparison demonstrates that, even with fixed orientations, optimization of part segmentation can further reduce the distortion objective.

We further analyze the effect of the number of sub-parts on distortion minimization by prescribing $N_P = 3, 4, \text{ and } 5$. The orientation variables for all sub-parts are set to $\pi/2$. The optimized segmentation and predicted distortion are shown in Fig. 12. The results indicate that as the prescribed number of sub-parts increases, the distortion objective decreases. This reduction in distortion occurs as the optimization breaks the layers into shorter segments. We note that a larger number of sub-parts may not be favourable from a manufacturing perspective, as it necessitates more frequent adjustments at the transitions between sub-parts. Additionally, more complex sub-parts may increase the risk of collision issues. With more sub-parts and shorter layer lengths, the number of layers to be deposited increases, consequently raising manufacturing time. For example, the total inter-layer cooling time, required to achieve the desired temperature across all layers, is proportional to the number of layers.

The final optimization option is the simultaneous optimization of both orientation and segmentation, providing maximum design flexibility. Figure 13 shows the results. In the upper row, simultaneous optimization is performed with $N_P = 2$. Comparing this with Fig. 10c, we observe that the simultaneously optimized result closely resembles that of the

sequential optimization, while achieving a 3.1% reduction in the objective function. When the part is segmented into four sub-parts, as shown in the bottom row, the objective function is further minimized.

The optimization process is computationally intensive, as each iteration requires evaluating the distortion introduced by every added layer, along with sensitivity analysis. The number of linear solver calls scales with the total number of layers, counting all sub-parts. In the numerical example of Fig. 13, with $N_P = 4$ sub-parts and 120 layers in total, on a finite element grid of 160×160 (52,164 DOFs for the complete part), the wall-clock time is approximately 11 hours.

4.2 Manufacturability considerations

In the results presented in Fig. 13, the segmentation lines appear highly curved. Such curved lines lead to shorter layers at the interface, which helps to reduce the distortion objective. However, excessive curvature can create fabrication challenges, particularly regarding accessibility. To address this, we extend the framework to allow control over the shape of the segmentation lines. The key idea is to align each segmentation line with the printing direction of the subsequent sub-part. Here, the orientation of the segmentation line is derived from the gradients of the pseudo-time field, or equivalently, from the temperature gradients.

Let $\nabla\mathbf{T}$ denote the gradient of the temperature field. The unit vectors \mathbf{v} , oriented along the gradient direction, are obtained by normalizing $\nabla\mathbf{T}$:

$$\mathbf{v} = \frac{\nabla\mathbf{T}}{(\|\nabla\mathbf{T}\|_2^2 + \epsilon)^{1/2}}. \quad (23)$$

Here, ϵ is a small positive constant introduced to prevent numerical instability when the gradient magnitude approaches zero. A default value of 1×10^{-9} is used. Figure 14a shows the unit vectors for the case of $N_P = 2$ in Fig. 13.

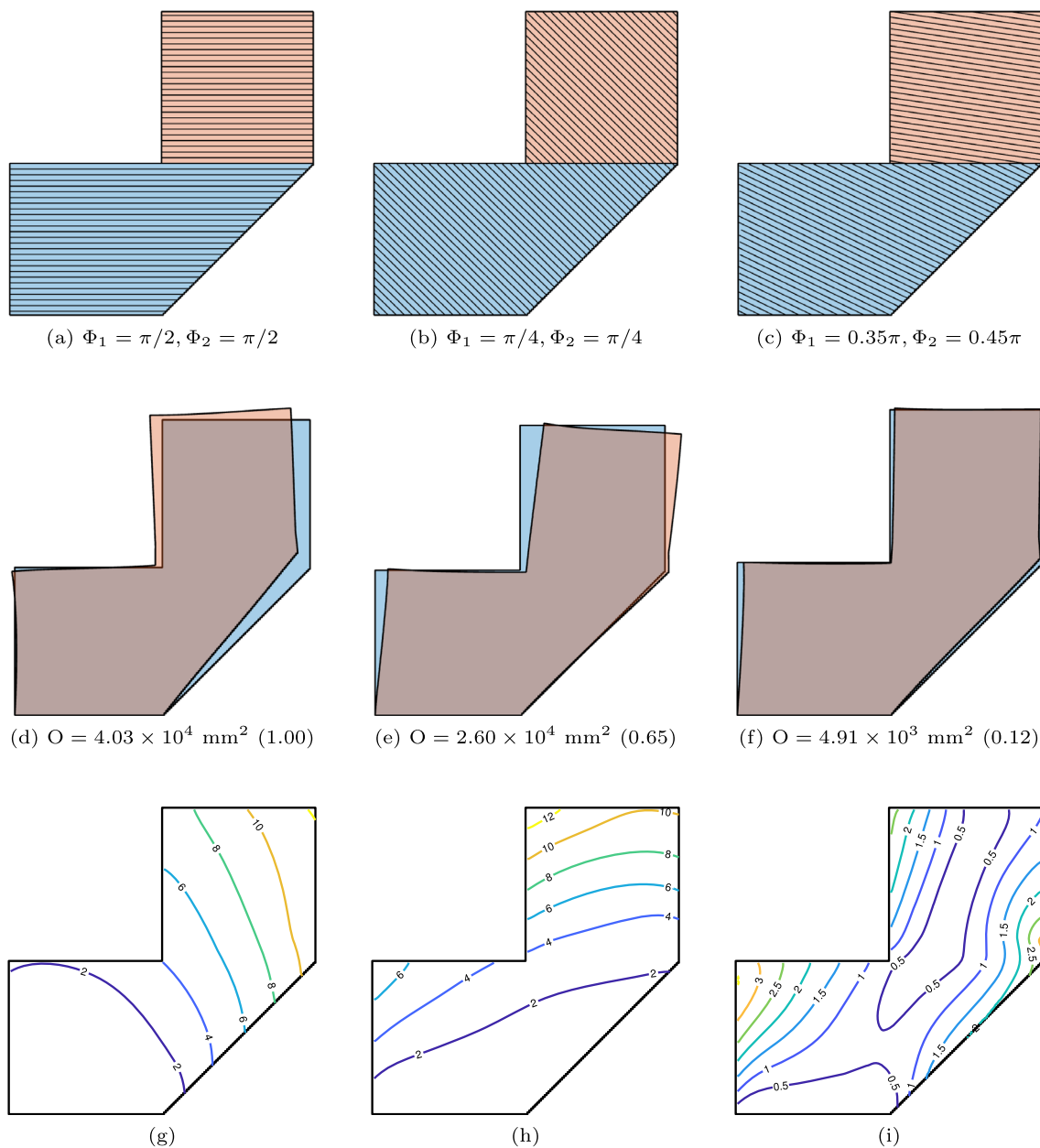


Fig. 10 Optimization of layer orientations under a fixed segmentation. **a** and **b** illustrate two different reference orientations, while **c** presents the optimized orientations. The middle and bottom rows display the corresponding distorted shape and contour plots of accumulated distortion

Next, we extract a narrow band of elements located near the segmentation line (B_i) and within the subsequent subpart. This band consists of elements whose pseudo-time values lie between τ_i and $\tau_i + \delta$, where δ is a positive constant with a default value of 0.1. In a differentiable manner, this set of elements is defined as

$$\mathbf{E}_{B_i} = \mathbf{B}(\boldsymbol{\tau}, \tau_i + \delta) - \mathbf{B}(\boldsymbol{\tau}, \tau_i), \tag{24}$$

where $\mathbf{B}(\boldsymbol{\tau}, \tau_i)$ denotes a smooth projection function. This projection maps values in $\boldsymbol{\tau}$ that are smaller than τ_i to 1 and values greater than τ_i to 0, and is given by

$$\mathbf{B}(\boldsymbol{\tau}, \tau_i) = \frac{\tanh(k_3 \tau_i) + \tanh(k_3(\boldsymbol{\tau} - \tau_i))}{\tanh(k_3 \tau_i) + \tanh(k_3(\mathbf{1} - \tau_i))} \tag{25}$$

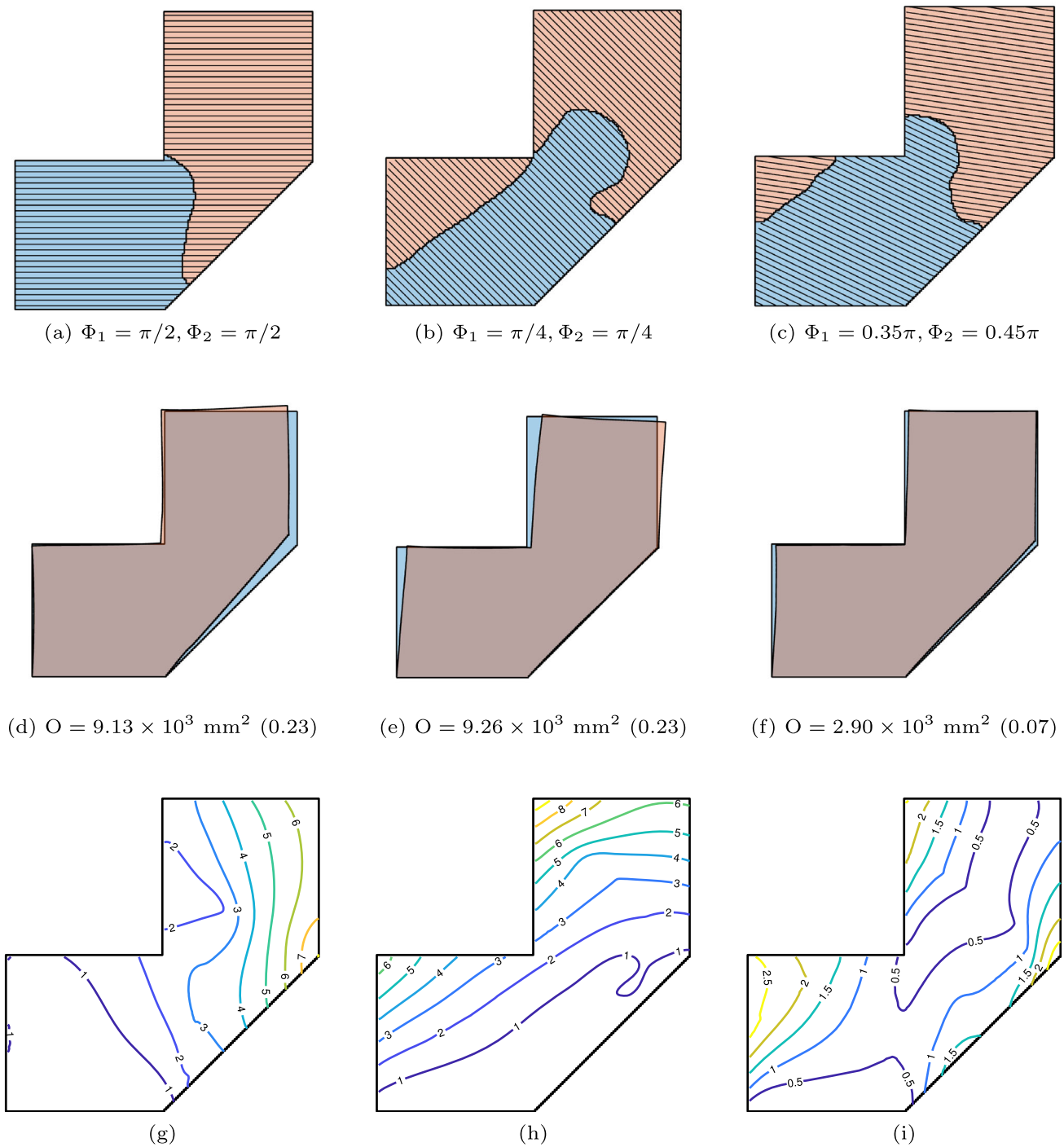
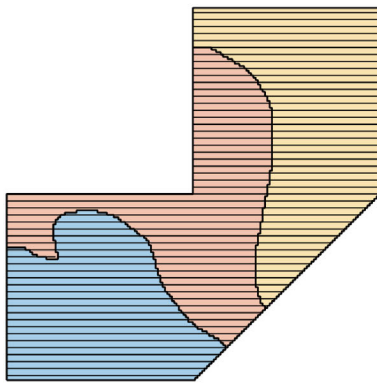


Fig. 11 Optimization of segmentation under prescribed orientations. Top row: Optimized segmentation with the orientations taken from Fig. 10. Middle row: The corresponding distorted shapes. Bottom row: The contour plots of accumulated distortion

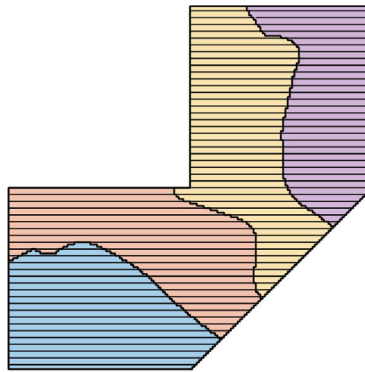
where the parameter k_3 controls the sharpness of the transition, with a default value of 100. Figure 14b illustrates \mathbf{E}_{B_i} , highlighting the elements located adjacent to the segmentation line. The thickness of this band varies along the line: regions with smaller temperature gradient magnitudes produce thicker bands. Nevertheless, uniform thickness is not

required for the formulation to function effectively. The corresponding unit gradient vectors within these regions are shown in Fig. 14c.

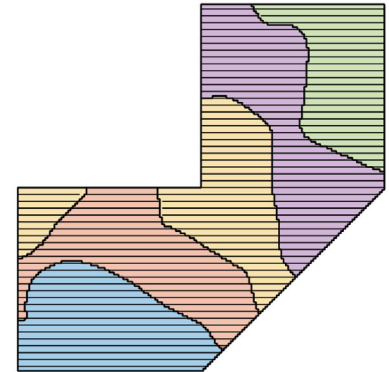
We introduce a metric to quantify the degree of (mis) alignment between the orientation of the segmentation line and the printing direction of the subsequent sub-part. Specif-



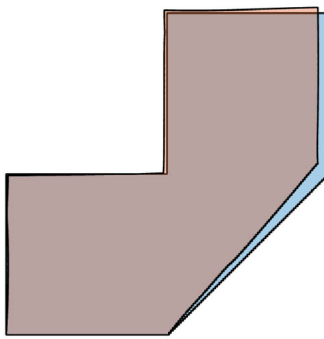
(a) $N_p = 3$



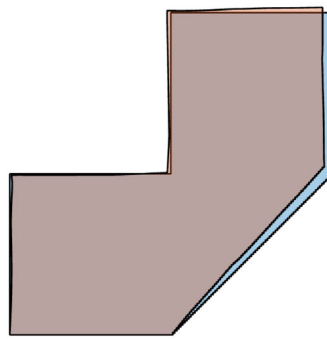
(b) $N_p = 4$



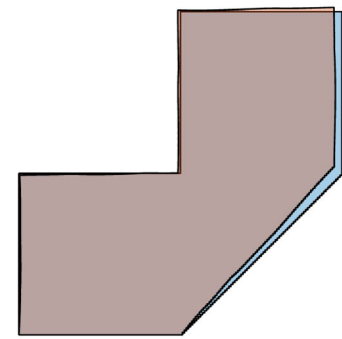
(c) $N_p = 5$



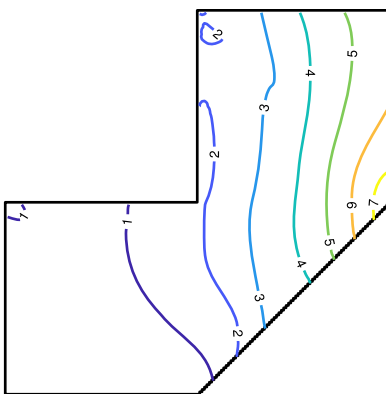
(d) $O = 6.31 \times 10^3 \text{ mm}^2$ (0.16)



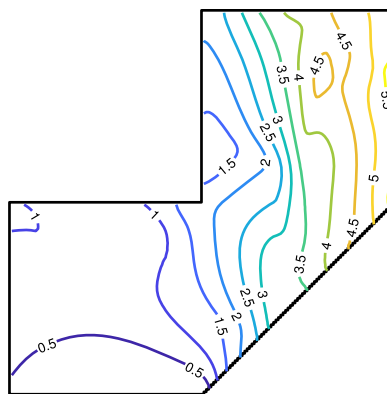
(e) $O = 5.16 \times 10^3 \text{ mm}^2$ (0.13)



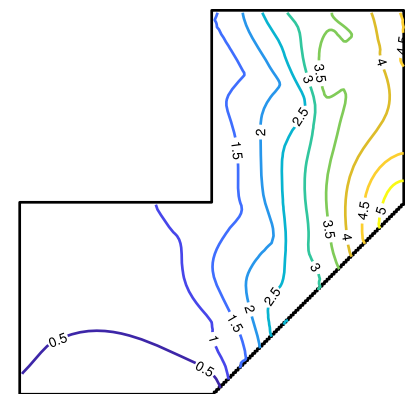
(f) $O = 3.73 \times 10^3 \text{ mm}^2$ (0.09)



(g)



(h)



(i)

Fig. 12 Segmentation is optimized under prescribed orientations, with the number of sub-parts increasing from left to right (3, 4, and 5, respectively). The top row presents the optimized segmentations, while the subsequent rows display the corresponding predicted distortions and their contour plots

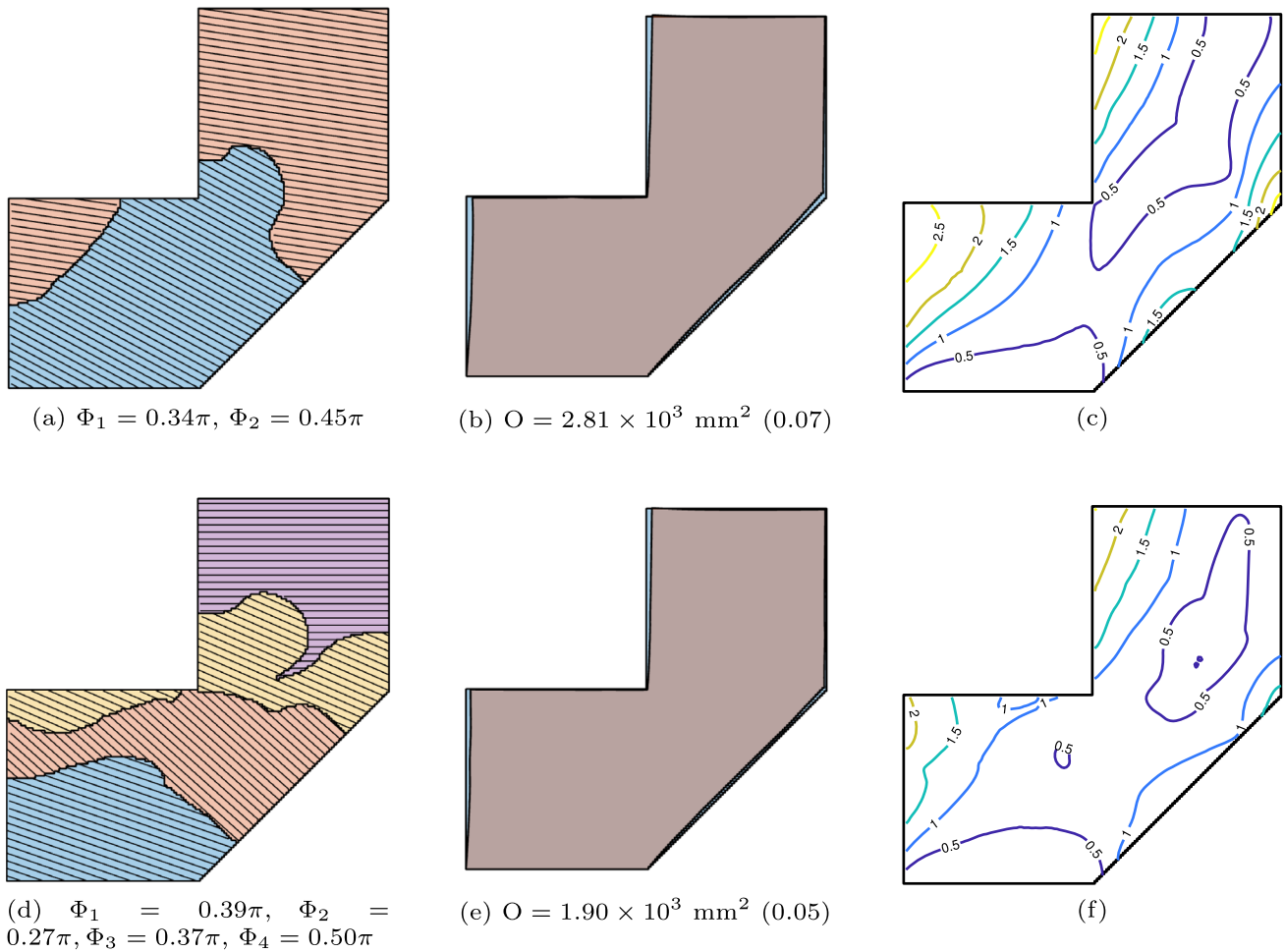


Fig. 13 Simultaneous optimization of segmentation and orientation, with $N_p = 2$ (a, b, c) and 4 (d, e, f)

ically, we compute the dot product between the thermal gradient vector (\mathbf{v}) and the printing direction vector ($\boldsymbol{\eta}_{\Phi_{i+1}}$). To localize this measure to the vicinity of the segmentation line, we apply a restriction to the relevant elements, yielding

$$\mathbf{C}_{\mathbf{B}_i} = \mathbf{E}_{\mathbf{B}_i} \circ (\mathbf{v} \cdot \boldsymbol{\eta}_{\Phi_{i+1}}). \tag{26}$$

The values of $\mathbf{C}_{\mathbf{B}_i}$ are predominantly negative, as the thermal gradients generally point in the opposite direction to the printing direction. The distribution of $\mathbf{C}_{\mathbf{B}_i}$ for the illustrative example is presented in Fig. 14d.

To enhance manufacturability, we introduce an additional objective that complements the primary objective of distortion minimization. Specifically, we incorporate the following terms into the objective function:

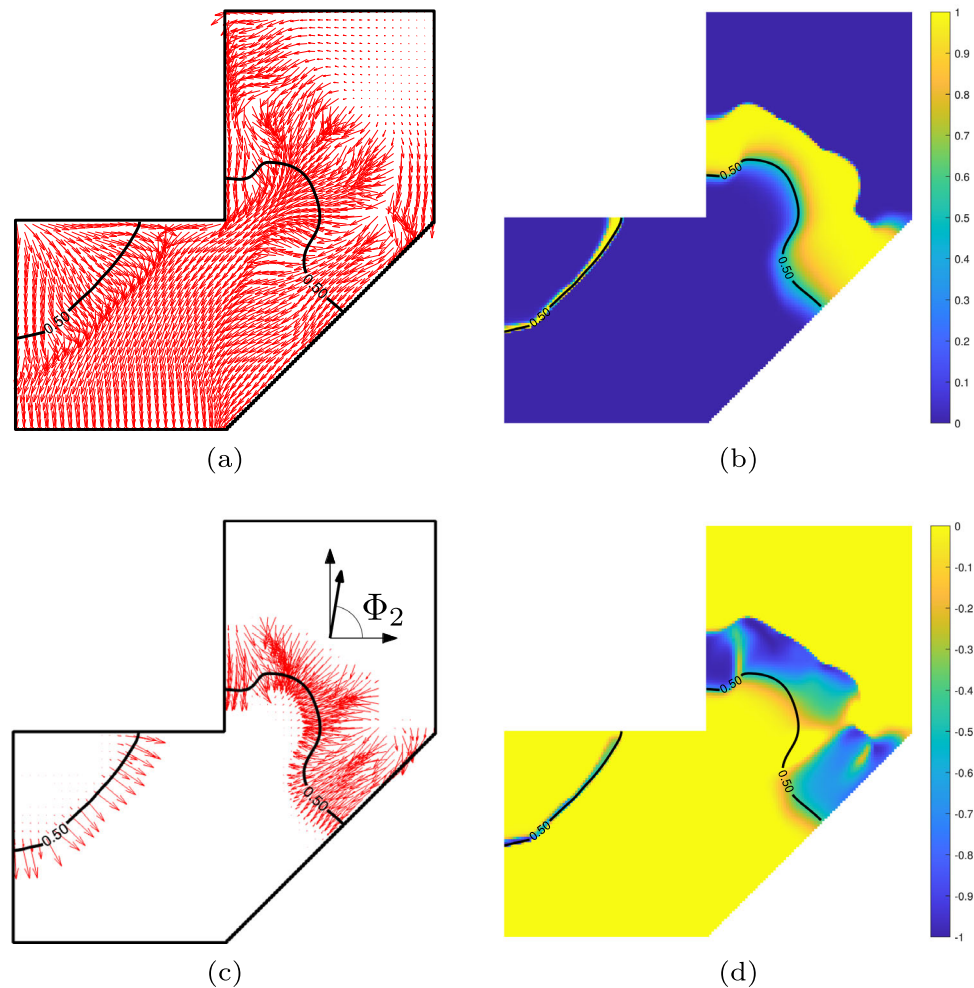
$$O_T = \mathbf{1}^T \mathbf{C}_{\mathbf{B}_i} + \mathbf{1}^T \mathbf{E}_{\mathbf{B}_i}, \tag{27}$$

where the first term represents the aggregated misalignment between the thermal gradients and the orientation variable.

Minimizing this term promotes the alignment of the segmentation line with the printing direction. The second term aggregates the elements identified in the vicinity of the segmentation line. By minimizing this term, the total length of the segmentation line is reduced. This is important because, without such a penalty, the optimization may produce excessively long and curved segmentation lines to generate short layers, which are thermally favorable for reducing distortion. Additionally, the second term influences the magnitude of the thermal gradient, as it affects the thickness of the identified band around the segmentation line.

The manufacturability objective is incorporated alongside the distortion minimization objective. The impact of this combined formulation for $N_p = 2$ and $N_p = 4$ is illustrated in Fig. 15. Compared to the baseline case shown in Fig. 13, the resulting segmentation lines exhibit reduced curvature and avoid sharp concave regions that would otherwise pose accessibility challenges.

Fig. 14 **a** Unit vectors along gradients calculated from the PDE-regularized field, **v**. **b** Region identified close to the segmentation line, \mathbf{E}_{B_1} . **c** The unit vectors of the gradients close the segmentation line. **d** Distribution of the inner product of the unit vectors of the gradients and the orientation variable, \mathbf{C}_{B_1}



4.3 More examples

Further test cases are shown in Fig. 16, where the objective function has been augmented with the manufacturability considerations. We acknowledge that the chosen shapes can be fabricated without a multi-planar deposition strategy. For example, the overhang (EX03) and underhang (EX04) can be reoriented and produced using a conventional planar layer-by-layer approach. However, these shapes were selected to demonstrate the robustness of the optimization method.

Figure 17 shows the optimized multi-planar strategies and corresponding predicted distortion, with $N_P = 2$ (first and second rows) and $N_P = 4$ (third and fourth rows). In all cases, the distorted shape (orange) closely aligns with the reference geometry (blue), demonstrating the effectiveness of the optimization approach. The objective function values in the brackets for $N_P = 4$ cases represent the normalized objective function values against their respective cases with $N_P = 2$. The proposed formulation successfully addresses critical geometric features encountered during the AM pro-

cess. This is most noticeable in the overhang (EX03) and underhang (EX04) cases with $N_P = 2$. In both cases, a sub-part is formed by introducing a segmentation line near the top-left end of the horizontal overhanging region. The optimized layer orientation in the second sub-part makes the part more self-supporting, as numerical simulations reveal that horizontal overhangs lead to significant distortion. Furthermore, a difference in layer orientation can be observed between the overhanging regions in (EX03) and (EX04). The latter represents a more challenging scenario, for which the minimum allowable value of the orientation variable during optimization is modified from its default of 0 to $-\pi/2$. This adjustment results in an optimized layer orientation that better accommodates the underhanging feature.

Lastly, Fig. 18a illustrates the convergence behavior of the distortion objective for the numerical examples with $N_P = 2$. The objective function values are normalized against their initial values from the first optimization step, providing a basis for comparing the examples and a clear measure of improvement in each example. Similarly, Fig. 18b depicts the

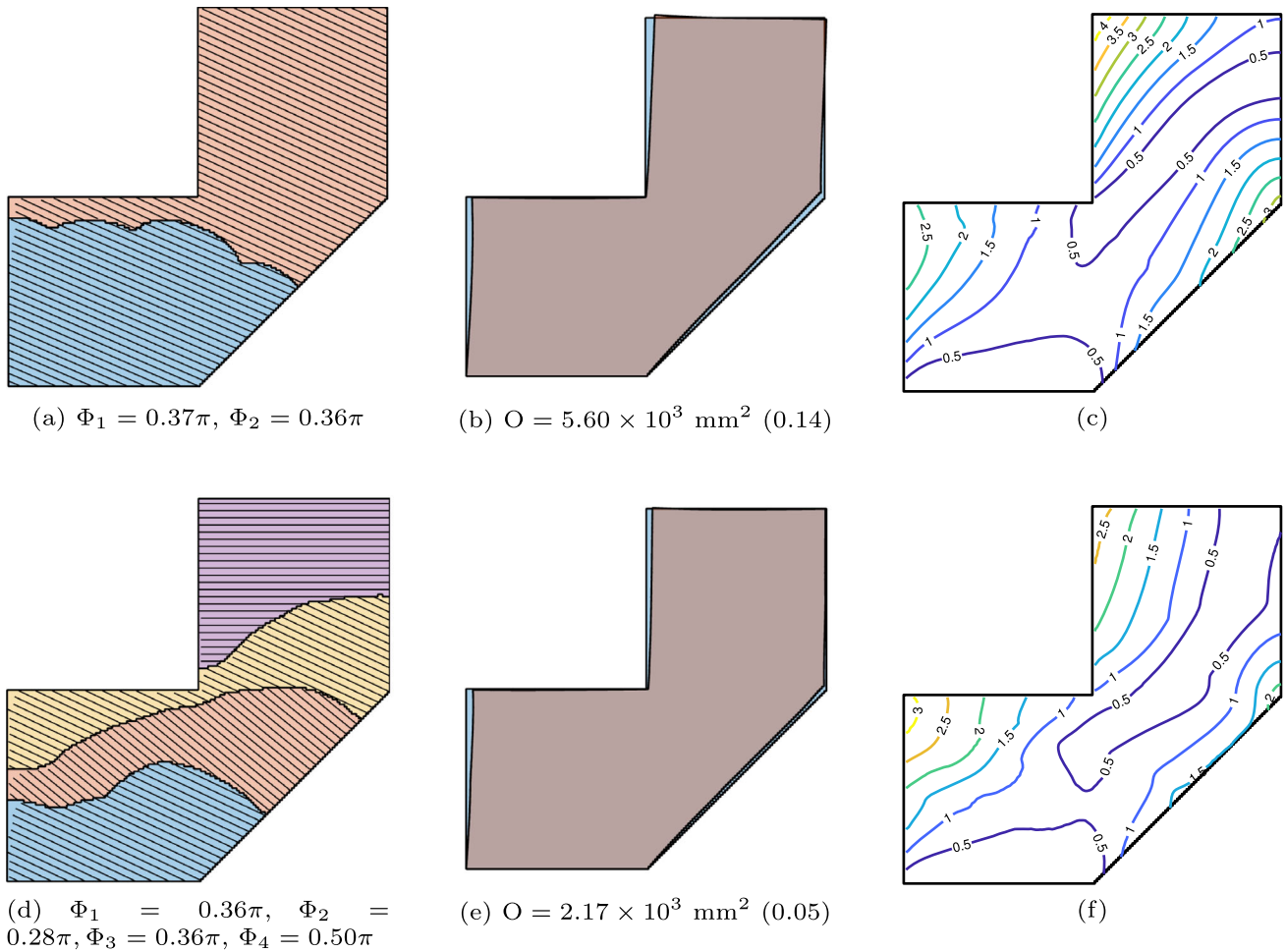


Fig. 15 Simultaneous optimization of segmentation and orientation, with $N_p = 2$ (a, b, c) and 4 (d, e, f), considering manufacturability objective

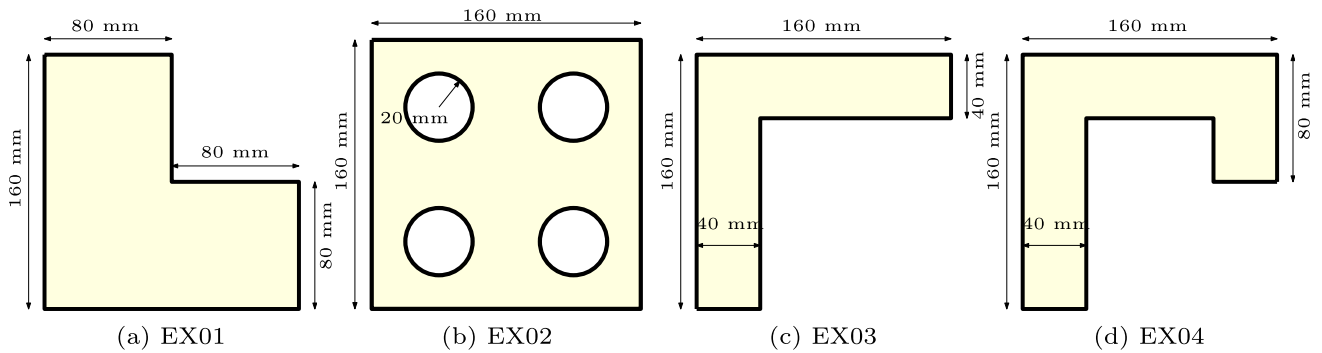


Fig. 16 Parts of varying complexity for testing the proposed optimization framework

evolution of the volume constraint for each sub-part. While the constraint is initially unsatisfied, the optimization process progressively adjusts the segmentation, leading to constraint satisfaction in most cases. We observed that, in two examples, the volume constraint per sub-part was not fully satisfied at

the end of the optimization. While some tuning of the optimization parameters could address this, it does not appear to be critical for practical applications. An interesting direction for future work would be to determine the volume of each sub-part through optimization.

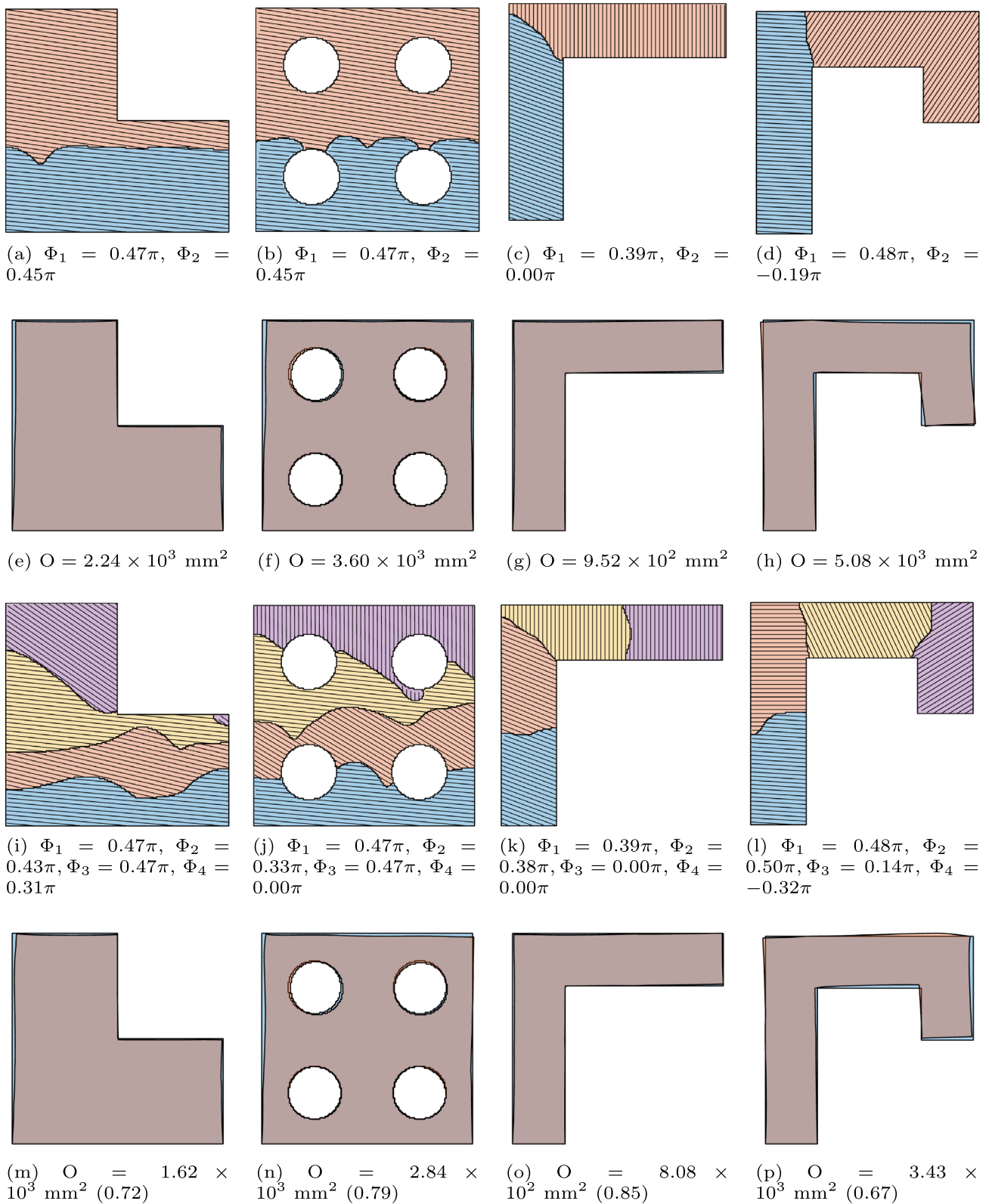


Fig. 17 Simultaneous optimization of segmentation and orientation, with $N_p = 2$ (first and second rows) and $N_p = 4$ (third and fourth rows)

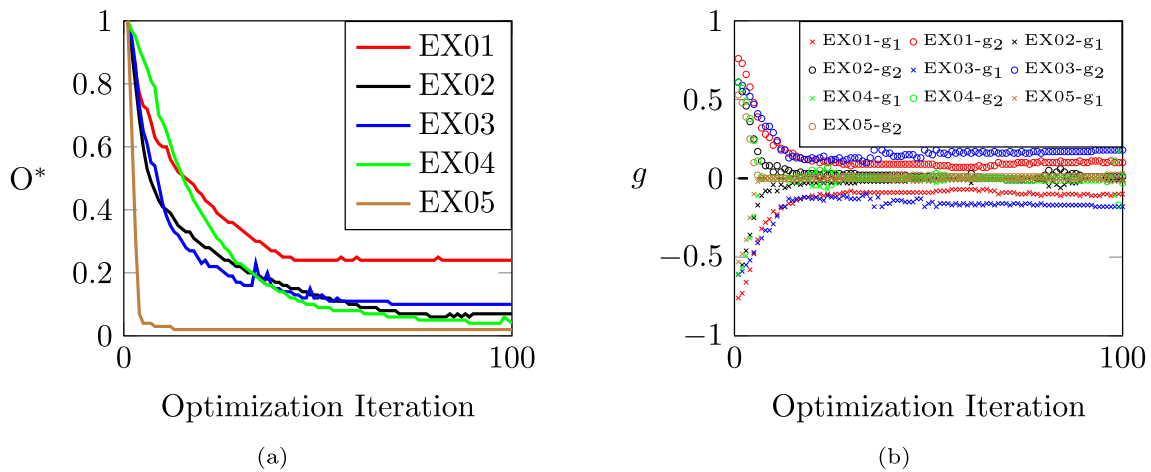


Fig. 18 Convergence behavior of the objective function for the numerical examples with $N_p = 2$

5 Conclusions

In this paper, we have presented a differentiable formulation for multi-planar slicing. This approach is inspired by recent advances in multi-axis additive manufacturing, which allows for the printing of each sub-part with a distinct printing direction. The multi-planar slicing strategy is parameterized by an orientation field and a pseudo-time field. The latter facilitates the segmentation of the part into a prescribed number of sub-parts. The formulation is applied to minimize distortion in wire arc additive manufacturing, using the inherent strain method as a simplified process model. The numerical results are encouraging. They confirm that both the printing direction and segmentation significantly influence distortion. The simultaneous optimization effectively utilizes this flexibility, resulting in a tenfold reduction in thermally induced distortion compared to the conventional planar approach.

The multi-planar strategy significantly reduces thermally induced distortion compared to conventional planar printing, while maintaining lower manufacturing complexity than curved fabrication (Wang et al. 2023). A potential manufacturing challenge arises from the emergence of curved segmentation lines. In this work, we addressed accessibility by promoting alignment between segmentation lines and the printing direction of subsequent sub-parts, as well as by minimizing their length. More research is needed to investigate further the implications of these curved segmentation lines and to develop strategies to regulate their geometry for improved manufacturability, such as considering the tool size.

Appendix A Sensitivity analysis

The objective function is

$$O = \sum_{i=1 \dots N_p} \sum_{j=j_{\min} \dots j_{\max}} \left[\Delta \mathbf{u}_{L_{ij}}^{P_i} \right]^T \left[\Delta \mathbf{u}_{L_{ij}}^{P_i} \right]. \tag{A1}$$

Differentiating with respect to the variable ξ_e gives

$$\frac{\partial O}{\partial \xi_e} = \sum_{i=1 \dots N_p} \sum_{j=j_{\min} \dots j_{\max}} 2 \left[\Delta \mathbf{u}_{L_{ij}}^{P_i} \right]^T \left[\frac{\partial \Delta \mathbf{u}_{L_{ij}}^{P_i}}{\partial \xi_e} \right]. \tag{A2}$$

The term $\left[\frac{\partial \Delta \mathbf{u}_{L_{ij}}^{P_i}}{\partial \xi_e} \right]$ is computationally expensive to calculate due to a large number of design variables (ξ_e). Therefore, an adjoint method is used here. Differentiating the state equation with respect to ξ_e gives

$$\left[\lambda_{L_{ij}}^{P_i} \right]^T \left[\frac{\partial \mathbf{K}_{L_{ij}}^{P_i}}{\partial \xi_e} \Delta \mathbf{u}_{L_{ij}}^{P_i} + \mathbf{K}_{L_{ij}}^{P_i} \frac{\partial \Delta \mathbf{u}_{L_{ij}}^{P_i}}{\partial \xi_e} - \frac{\partial \mathbf{F}_{L_{ij}}^{P_i}}{\partial \xi_e} \right] = \mathbf{0}. \tag{A3}$$

Adding Eq. (A3) in Eq. (A2), and after simplification we get

$$\frac{\partial O}{\partial \xi_e} = \sum_{i=1 \dots N_p} \sum_{j=1 \dots N_L} \left[\lambda_{L_{ij}}^{P_i} \right]^T \left[\frac{\partial \mathbf{K}_{L_{ij}}^{P_i}}{\partial \xi_e} \Delta \mathbf{u}_{L_{ij}}^{P_i} - \frac{\partial \mathbf{F}_{L_{ij}}^{P_i}}{\partial \xi_e} \right]. \tag{A4}$$

The Lagrange multiplier is calculated by solving the adjoint equation,

$$\mathbf{K}_{L_{ij}}^{P_i} \lambda_{L_{ij}}^{P_i} = -2 \Delta \mathbf{u}_{L_{ij}}^{P_i}. \tag{A5}$$

The sensitivity terms required to be evaluated are $\frac{\partial \mathbf{K}_{Lij}^{P_i}}{\partial \xi_e}$ and $\frac{\partial \mathbf{F}_{Lij}^{P_i}}{\partial \xi_e}$. Applying the chain rule, these terms can be written as

$$\frac{\partial \mathbf{K}_{Lij}^{P_i}}{\partial \xi_e} = \frac{\partial \mathbf{K}_{Lij}^{P_i}}{\partial \mathbf{D}_{Lij}^{P_i}} \frac{\partial \mathbf{D}_{Lij}^{P_i}}{\partial \tau} \frac{\partial \tau}{\partial \xi_e}, \quad (\text{A6})$$

$$\frac{\partial \mathbf{F}_{Lij}^{P_i}}{\partial \xi_e} = \frac{\partial \mathbf{F}_{Lij}^{P_i}}{\partial \mathbf{E}_{Lij}^{P_i}} \frac{\partial \mathbf{E}_{Lij}^{P_i}}{\partial \tau} \frac{\partial \tau}{\partial \xi_e}. \quad (\text{A7})$$

The term $\frac{\partial \tau}{\partial \xi_e}$ is evaluated as

$$\frac{\partial \tau}{\partial \xi_e} = -\mathbf{A} \frac{\partial \mathbf{T}}{\partial \xi_e}. \quad (\text{A8})$$

The adjoint method is used to evaluate $\frac{\partial \mathbf{T}}{\partial \xi_e}$. The state equation is differentiated as

$$\left[\lambda_{\mathbf{T}} \right]^T \left[\frac{\partial \mathbf{K}_{\mathbf{T}}}{\partial \xi_e} \mathbf{T} + \mathbf{K}_{\mathbf{T}} \frac{\partial \mathbf{T}}{\partial \xi_e} - \frac{\partial \mathbf{b}}{\partial \xi_e} \right] = \mathbf{0}. \quad (\text{A9})$$

Since the heat load is independent of the design variable, i.e., $\frac{\partial \mathbf{b}}{\partial \xi_e} = \mathbf{0}$, the above equation reduces to

$$\left[\lambda_{\mathbf{T}} \right]^T \left[\frac{\partial \mathbf{K}_{\mathbf{T}}}{\partial \xi_e} \mathbf{T} + \mathbf{K}_{\mathbf{T}} \frac{\partial \mathbf{T}}{\partial \xi_e} \right] = \mathbf{0}. \quad (\text{A10})$$

Now adding the above equation to Eq. (A8) and simplifying it leads to

$$\frac{\partial \tau}{\partial \xi_e} = -\mathbf{A} \frac{\partial \mathbf{T}}{\partial \xi_e} + \left[\lambda_{\mathbf{T}} \right]^T \left[\frac{\partial \mathbf{K}_{\mathbf{T}}}{\partial \xi_e} \mathbf{T} + \mathbf{K}_{\mathbf{T}} \frac{\partial \mathbf{T}}{\partial \xi_e} \right]. \quad (\text{A11})$$

To evaluate the multiplier $\lambda_{\mathbf{T}}$, we isolate the term of $\frac{\partial \mathbf{T}}{\partial \xi_e}$ and form the adjoint equation as

$$\mathbf{K}_{\mathbf{T}} \lambda_{\mathbf{T}} = \mathbf{A}^T. \quad (\text{A12})$$

The sensitivity of the term $\frac{\partial \tau}{\partial \xi_e}$ is given as

$$\frac{\partial \tau}{\partial \xi_e} = \left[\lambda_{\mathbf{T}} \right]^T \left[\frac{\partial \mathbf{K}_{\mathbf{T}}}{\partial \xi_e} \mathbf{T} \right]. \quad (\text{A13})$$

Author Contributions Vibhas Mishra: Conceptualization, Methodology, Writing - original draft. Jun Wu: Conceptualization, Methodology, Writing - review & editing, Supervision, Funding acquisition.

Funding This work is partially supported by the Dutch Research Council (NWO), The Netherlands, with project number 20382 (*Space-TimeOpt*), and project number NWA.1418.24.053 (*AM4Micro*).

Data availability The relevant data, materials, and code will be made available upon publication of the article or can be provided upon request.

Declarations

Conflict of interest The authors have no relevant financial or non-financial interests to disclose.

Replication of Results The authors have explained the procedure to replicate the results and intend to release the code upon publication of the article.

Ethics approval All authors consent to publication.

Open Access This article is licensed under a Creative Commons Attribution 4.0 International License, which permits use, sharing, adaptation, distribution and reproduction in any medium or format, as long as you give appropriate credit to the original author(s) and the source, provide a link to the Creative Commons licence, and indicate if changes were made. The images or other third party material in this article are included in the article's Creative Commons licence, unless indicated otherwise in a credit line to the material. If material is not included in the article's Creative Commons licence and your intended use is not permitted by statutory regulation or exceeds the permitted use, you will need to obtain permission directly from the copyright holder. To view a copy of this licence, visit <http://creativecommons.org/licenses/by/4.0/>.

References

- Allaire G, Jakabčič L (2018) Taking into account thermal residual stresses in topology optimization of structures built by additive manufacturing. *Math Models Methods Appl Sci* 28(12):2313–2366. <https://doi.org/10.1142/S0218202518500501>
- Bendsøe MP, Sigmund O (2004) *Topology Optimization: Theory, Methods, and Applications*. Springer, Berlin, Heidelberg. <https://doi.org/10.1007/978-3-662-05086-6>
- Bi D, Duan M, Lau TY, Xie F, Tang K (2023) Strength-enhanced volume decomposition for multi-directional additive manufacturing. *Addit Manuf* 69:103529. <https://doi.org/10.1016/j.addma.2023.103529>
- Chen Q, Liang X, Hayduke D, Liu J, Cheng L, Oskin J, Whitmore R, To AC (2019) An inherent strain based multiscale modeling framework for simulating part-scale residual deformation for direct metal laser sintering. *Addit Manuf* 28:406–418. <https://doi.org/10.1016/j.addma.2019.05.021>
- Dai C, Wang CC, Wu C, Lefebvre S, Fang G, Liu Y-J (2018) Support-free volume printing by multi-axis motion. *ACM Transa Graph* 37(4):1–14. <https://doi.org/10.1145/3197517.3201342>
- Elmer JW, Fisher K, Gibbs G, Sengthay J, Urabe D (2022) Post-build thermomechanical processing of wire arc additively manufactured stainless steel for improved mechanical properties and reduction of crystallographic texture. *Addit Manuf* 50:102573. <https://doi.org/10.1016/j.addma.2021.102573>
- Gao Y, Wu L, Yan D-M, Nan L (2019) Near support-free multi-directional 3d printing via global-optimal decomposition. *Graph Models* 104:101034. <https://doi.org/10.1016/j.gmod.2019.101034>
- Guo Y, Liu J, Ahmad R, Ma Y (2025) Concurrent structural topology and fabrication sequence optimization for multi-axis additive man-

- ufacturing. *Comput Methods Appl Mech Eng* 435:117627. <https://doi.org/10.1016/j.cma.2024.117627>
- Jafari D, Vaneker TH, Gibson I (2021) Wire and arc additive manufacturing: opportunities and challenges to control the quality and accuracy of manufactured parts. *Mater Design* 202:109471. <https://doi.org/10.1016/j.matdes.2021.109471>
- Jiang X, Cheng X, Peng Q, Liang L, Dai N, Wei M, Cheng C (2017) Models partition for 3d printing objects using skeleton. *Rapid Prototyping J* 23(1):54–64. <https://doi.org/10.1108/RPJ-07-2015-0091>
- Lettori J, Raffaelli R, Bilancia P, Peruzzini M, Pellicciari M (2022) A review of geometry representation and processing methods for cartesian and multiaxial robot-based additive manufacturing. *Int J Adv Manuf Technol* 123(11):3767–3794. <https://doi.org/10.1007/s00170-022-10432-8>
- Liang X, Chen Q, Cheng L, Hayduke D, To AC (2019) Modified inherent strain method for efficient prediction of residual deformation in direct metal laser sintered components. *Comput Mech* 64:1719–1733. <https://doi.org/10.1007/s00466-019-01748-6>
- Livesu M, Ellero S, Martínez J, Lefebvre S, Attene M (2017) From 3d models to 3d prints: an overview of the processing pipeline. *Comput Graph Forum* 36(2):537–564. <https://doi.org/10.1111/cgf.13147>
- Luo L, Baran I, Rusinkiewicz S, Matusik W (2012) Chopper: Partitioning models into 3d-printable parts. *ACM Transa Graph (TOG)* 31(6):1–9. <https://doi.org/10.1145/2366145.2366148>
- Ma N, Nakacho K, Ohta T, Ogawa N, Maekawa A, Huang H, Murakawa H (2016) Inherent strain method for residual stress measurement and welding distortion prediction. *Int Conf Offshore Mech Arctic Eng* 50008:009–13001. <https://doi.org/10.1115/OMAE2016-54184>
- Miki T, Yamada T (2021) Topology optimization considering the distortion in additive manufacturing. *Finite Elem Anal Des* 193:103558. <https://doi.org/10.1016/j.finel.2021.103558>
- Misiun G, Ven E, Langelaar M, Geijselaers H, Keulen F, Boogaard T, Ayas C (2021) Topology optimization for additive manufacturing with distortion constraints. *Comput Methods Appl Mech Eng* 386:114095. <https://doi.org/10.1016/j.cma.2021.114095>
- Munro D, Ayas C, Langelaar M, Keulen F (2019) On process-step parallel computability and linear superposition of mechanical responses in additive manufacturing process simulation. *Addit Manuf* 28:738–749. <https://doi.org/10.1016/j.addma.2019.06.023>
- Murtezaoglu Y, Plakhotnik D, Stautner M, Vaneker T, Houten FJ (2018) Geometry-based process planning for multi-axis support-free additive manufacturing. *Procedia Cirp* 78:73–78. <https://doi.org/10.1016/j.procir.2018.08.175>
- Oh Y, Zhou C, Behdad S (2018) Part decomposition and assembly-based (re) design for additive manufacturing: A review. *Addit Manuf* 22:230–242. <https://doi.org/10.1016/j.addma.2018.04.018>
- Pellens J, Lombaert G, Michiels M, Craeghs T, Schevenels M (2020) Topology optimization of support structure layout in metal-based additive manufacturing accounting for thermal deformations. *Struct Multidiscip Optim* 61(6):2291–2303. <https://doi.org/10.1007/s00158-020-02512-8>
- Prabhune BC, Suresh K (2020) A fast matrix-free elasto-plastic solver for predicting residual stresses in additive manufacturing. *Comput Aided Des* 123:102829. <https://doi.org/10.1016/j.cad.2020.102829>
- Rodrigues TA, Duarte V, Miranda RM, Santos TG, Oliveira JP (2019) Current status and perspectives on wire and arc additive manufacturing (waam). *Materials* 12(7):1121. <https://doi.org/10.3390/ma12071121>
- Shen H, Lin J, Zhou Z, Liu B (2022) Effect of induction heat treatment on residual stress distribution of components fabricated by wire arc additive manufacturing. *J Manuf Process* 75:331–345. <https://doi.org/10.1016/j.jmapro.2022.01.018>
- Singh P, Dutta D (2001) Multi-direction slicing for layered manufacturing. *J Comput Inf Sci Eng* 1(2):129–142. <https://doi.org/10.1115/1.1375816>
- Ueda Y, Fukuda K, Nakacho K, Endo S (1975) A new measuring method of residual stresses with the aid of finite element method and reliability of estimated values. *J Soc Naval Archit Japan* 1975(138):499–507. https://doi.org/10.2534/jjasnaoe1968.1975.138_499
- Wang W, Munro D, Wang CC, Keulen F, Wu J (2020) Space-time topology optimization for additive manufacturing: concurrent optimization of structural layout and fabrication sequence. *Struct Multidiscip Optim* 61:1–18. <https://doi.org/10.1007/s00158-019-02420-6>
- Wang W, Keulen F, Wu J (2023) Fabrication sequence optimization for minimizing distortion in multi-axis additive manufacturing. *Comput Methods Appl Mech Eng* 406:115899. <https://doi.org/10.1016/j.cma.2023.115899>
- Wang W, Wu K, Keulen F, Wu J (2024) Regularization in space-time topology optimization for additive manufacturing. *Comput Methods Appl Mech Eng* 431:117202. <https://doi.org/10.1016/j.cma.2024.117202>
- Wu C, Dai C, Fang G, Liu Y-J, Wang CC (2019) General support-effective decomposition for multi-directional 3-d printing. *IEEE Trans Autom Sci Eng* 17(2):599–610. <https://doi.org/10.1109/TASE.2019.2938219>
- Wu K, Wang W, Keulen F, Wu J (2024) Space-time topology optimization for anisotropic materials in wire and arc additive manufacturing. *Int J Mech Sci* 284:109712. <https://doi.org/10.1016/j.ijmecsci.2024.109712>
- Wu K, Keulen F, Wu J (2025) Residual stress-constrained space-time topology optimization for multi-axis additive manufacturing. *Comput Methods Appl Mech Eng* 440:117913. <https://doi.org/10.1016/j.cma.2025.117913>
- Wu C, Dai C, Fang G, Liu Y-J, Wang CC (2017) Robofdm: A robotic system for support-free fabrication using fdm. In: 2017 IEEE International Conference on Robotics and Automation (ICRA), pp. 1175–1180. <https://doi.org/10.1109/ICRA.2017.7989140>. IEEE
- Xiao X, Joshi S (2020) Process planning for five-axis support free additive manufacturing. *Addit Manuf* 36:101569. <https://doi.org/10.1016/j.addma.2020.101569>
- Xu K, Chen L, Tang K (2018) Support-free layered process planning toward 3+ 2-axis additive manufacturing. *IEEE Trans Autom Sci Eng* 16(2):838–850. <https://doi.org/10.1109/TASE.2018.2867230>
- Yao M, Chen Z, Luo L, Wang R, Wang H (2015) Level-set-based partitioning and packing optimization of a printable model. *ACM Transa Graph (TOG)* 34(6):1–11. <https://doi.org/10.1145/2816795.2818064>
- Zhang T, Fang G, Huang Y, Dutta N, Lefebvre S, Kilic ZM, Wang CC (2022) S3-slicer: a general slicing framework for multi-axis 3d printing. *ACM Transa Graph* 41(6):1–15. <https://doi.org/10.1145/3550454.3555516>

Publisher's Note Springer Nature remains neutral with regard to jurisdictional claims in published maps and institutional affiliations.